Comparison of Rotor Arrangements of Transverse Flux Machines for a Robotic Direct Drive optimized by Genetic Algorithm and Regression Tree Method

Benedikt Kaiser* [ID], Martin Schmid [ID], Nejila Parspour [ID]
Institute of Electrical Energy Conversion
University of Stuttgart
Stuttgart, Germany
*benedikt.kaiser@iew.uni-stuttgart.de

Abstract—Articulated robotics applications typically have a demand for high torque at low speed. However, conventional electrical machines cannot generate a reasonable amount of torque directly by electro-magnetics. Therefore, gearboxes are used to convert speed and torque, accepting loss of mechanical power due to additional friction. Although geared solutions for robotic drive trains already offer exceedingly high torque densities, they are limited by the drawbacks of high reduction gears, such as non-linearities in friction, complex flexibility effects, and limited service life of mechanics in contrary to direct drive solutions. The Transverse Flux Machine with the high gravimetric torque density may be a solution for reducing or eliminating the need for a gearbox. Using a genetic algorithm, the proposed Transverse Flux Machines are optimized. To enhance the optimization's speed, the machines' calculations done by Finite-Element-Analysis of selected generations are replaced by a Regression Tree Model whose results are verified after a defined expired model service life with a subsequent adjustment of the model. The eligibility of different arrangements the Transverse Flux Machines' rotor are compared regarding the application as low-speed direct drive in robotics, also compared to similar Radial Flux Machines. The optimized Transverse Flux Machines have a higher efficiency due to lower copper loss and a higher active gravimetric torque density. However, the Radial Flux Machines have higher total torques and power factors.

Index Terms—Direct drive, electric machines, modulated pole machines, permanent magnet machines, power factor, robotics, rotating machines, torque density, torque ripple, transverse flux machines.

I. INTRODUCTION

The inherent advantages of direct drives are an elimination of the non-linearities and uncertainties of high reduction gears [1], such as strain-wave gears and cycloid gears which are state-of-the-art in lightweight robotics applications. However, the size of an electrical machine increases with torque demand resulting in insufficient designs. Transverse Flux Machines (TFMs) are known for their high gravimetric torque density and high efficiency at low speed. Within this work, two types of TFMs are examined as a direct drive solution suited for the field of robotics.

Due to the complex 3D magnetic flux of the TFM, the optimization of a machine via multiple FEAs has high computational effort. This is especially critical in comparison with other topologies, such as the 2D-computed Radial Flux Machine (RFM) or the quasi 3D- or analytically computed Axial Flux Machine (AFM). For example, in [2] the non-optimized TFM has inferior electromagnetic properties compared to the optimized RFM and AFM, neglecting the possibilities of an optimized design of the TFM. A case study [3] related to the optimization of a TFM with surface mount permanent magnets and soft magnetic composite stator points out significant improvements of the optimized design referred to an initial design. Therefore, it is assumed that the full potential of TFMs has not been exploited yet. The study [4] presents a higher torque density of TFMs with an outer rotor design which also applies for conventional machines [5] due to the geometry of higher lever arm of the air gap with a typically lower height of the rotor compared to the stator. The in [6], [7] presented double stator machines present an intermediate solution which will be compared to the single stator designs in the following sections.

The intended reference application is a direct drive for the base axis of a lightweight articulated robot arm which is used for collaborative tasks such as the Franka Emika Panda robot with a software-set joint torque limit of $87\,\mathrm{N\,m}$ and maximum speed of $25\,\mathrm{min^{-1}}$ [8]. The assumed arising cylindrical installation space has an outer diameter of $d_\mathrm{o} = 180\,\mathrm{mm}$ and a length of $l_\mathrm{o} = 150\,\mathrm{mm}$, which is nearly double the volume of the of the Franka Emika Panda installation space (approx. $d_\mathrm{o} \approx 110\,\mathrm{mm}$, $l_\mathrm{o} \approx 200\,\mathrm{mm}$, based on CAD-measurement). A hollow shaft for routing cables and pipelines through the drive is an additional requirement. The cooling of the machine is passive only.

II. EXAMINED MACHINES

The evaluated machines are built of a three phase TFM with hoop coils, as displayed for the single phase segments in Fig. 1 (a)-(f). For the comparison, the arrangement of the stator as inner-stator (IS), outer-stator (OS), and double-stator (DS)

(a) Outer stator design (OS-UI-TFM)   (b) Inner stator design (IS-UI-TFM)   (c) Double stator design (DS-UI-TFM)

(d) Outer stator design (OS-CP-TFM)   (e) Inner stator design (IS-CP-TFM)   (f) Double stator design (DS-CP-TFM)
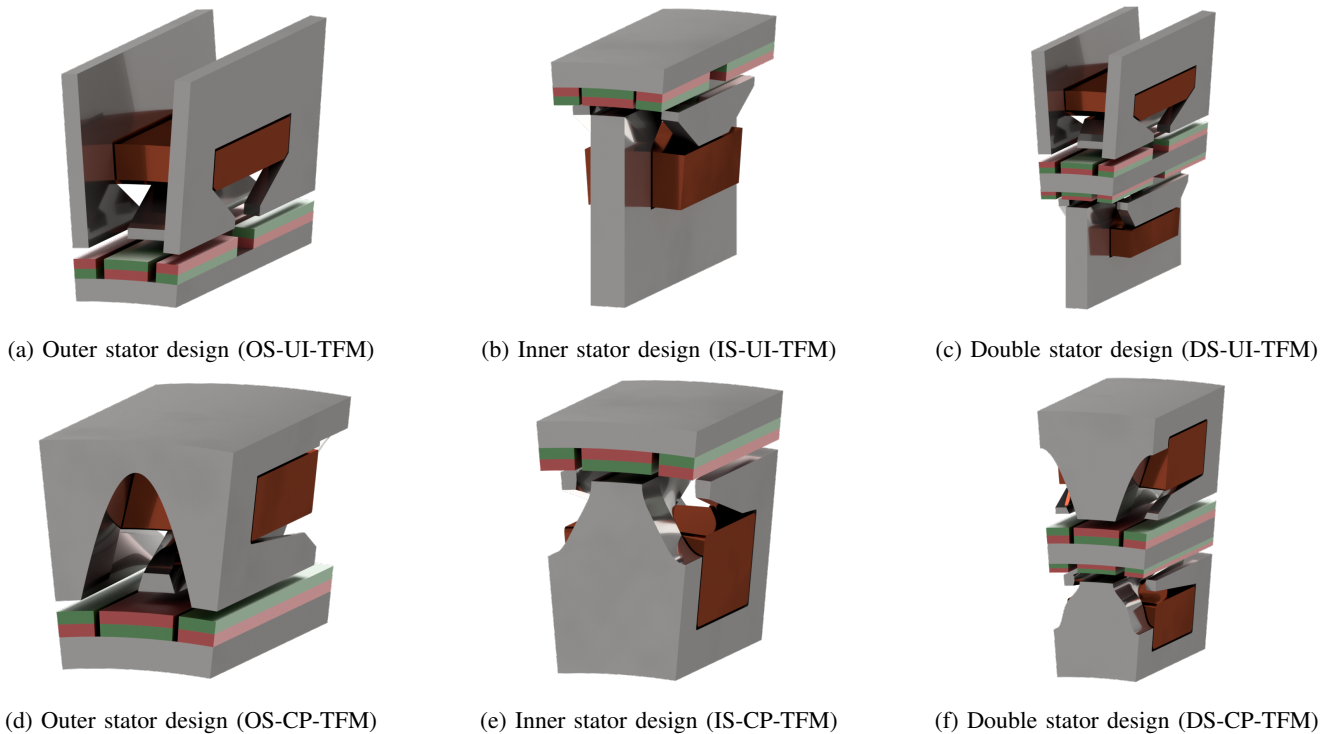
Figure 1: Arrangements of rotors and stators of the (a)-(c) UI- and (d)-(f) CP-TFMs for the comparison, already with selected geometry of optimization results demonstrated for a single phase and pole pair. Soft magnetics are displayed in gray, the conductor in copper, and the magnets in green/red.

is varied. Additionally, there are two designs of soft magnetic stator core investigated.

The structure of the first TFM stators' soft magentics is an UI-core, according to the definition in [9], with an adapted design for two-dimensional laminated steel (M250-35A). A similar construction is found in [10] for the application as a generator or in several publications of M.R. Harris et al., for instance [11]. The second investigated stator is a claw pole (CP) stator machine made of isotropic soft magnetic composite, similar to the machine presented in [12]. All machines have surface mount permanent magnet rotors with NdFeB Grade N42-SH with an assumed temperature of $80\,°\mathrm{C}$. In contrast to the previously mentioned machines of Gieras et al. and Harris et al., for the surface mount rotor coreback solid free-cutting steel 9S20K (material number 1.0711) is used instead of laminations, allowing 3D-magnetic flux but accepting higher iron loss due to eddy current.

For supplementary comparison with conventional machines, the optimization is performed for Radial Flux Machines as well (cut-view see Fig. 2). In order to have a comparative study, the simulation is performed in 2D with similar settings and properties. An exception is made by the choice of the material, all soft magnetics are defined as laminated steel (M250-35A). For a reduction of complexity in winding design, the number of pole pairs p and the number of slots n_S are proportionally linked $3 \cdot p = n_\mathrm{S}$ in order to have a concentrated winding scheme. This limits the usage of

combinations with higher winding factors, for instance the popular $p = 5$ and $n_\mathrm{S} = 12$ design.

III. Accelerated Simulation Model and Iron Loss Calculation

Using the periodicity of the pole pairs, the simulated geometry is reduced to only one pole pair. Due to the magnetic decoupling of the phases of the TFMs, the simulated geometry is reduced further to only one phase. For the magnetic decoupling an additional axial distance is assumed as five times air gap length between rotor and stator $(5 \cdot l_\delta)$. Because of the duration of 3D transient studies of the TFM's geometries, a faster multi-static (instead of transient) simulation approach with less degrees of freedom and iron loss calculation according to Bertotti in post-processing (presented in [13]) is used. This reduces the simulation time from hours to minutes allowing only an estimation of iron losses $P_{\mathrm{L,Fe}}$. Additionally, for the 3D loss calculation routine the coordinate transformation presented in [14] is utilized. In order to obtain the frequency and amplitude of higher harmonics of flux density and elimination of the DC-offset, the time domain flux density signal is transformed into a frequency signal by help of the Fast Fourier Transform (FFT) and accumulated up to the 12th-harmonic.

To achieve a shorter duration of single simulations, additional limitations are accepted, decreasing the precision of the

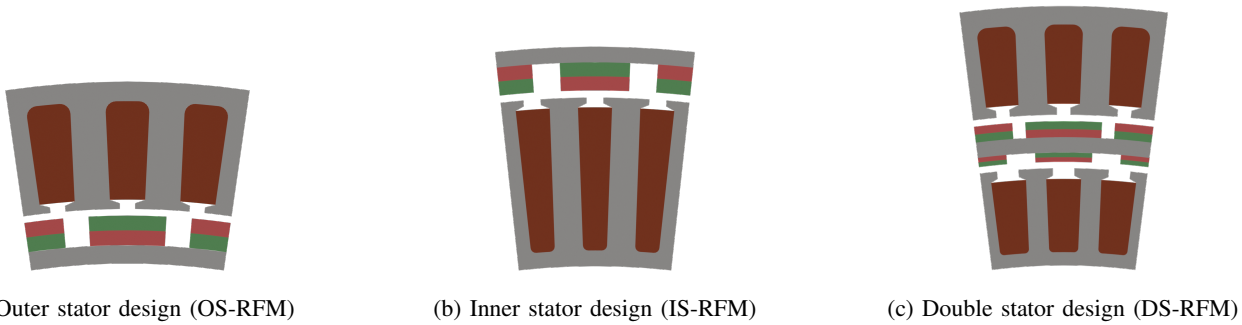(a) Outer stator design (OS-RFM)   (b) Inner stator design (IS-RFM)   (c) Double stator design (DS-RFM)

Figure 2: Cut-view of a pole pair of the RFMs for the comparison, with geometry of optimizations' selected results. Soft magnetics are displayed in gray, the conductor in copper, and the magnets in green/red.

calculated results. For a faster simulation, the 3D influence of the orientation of the lamination is neglected. For an accurate model, the modeling approach in [15] may be utilized, but due to the highly non-linear material the solving of the problem has a high computational effort and is not suited for this optimization problem with a large number of simulations. Additionally, because of the multi-static simulation, the influence of eddy current with feedback to the magnetics and the magnet loss is not modeled. The voltages of the coil terminals are calculated in post-processing utilizing the concatenated flux and the phase voltage equation. Mechanical constraints such as mechanical stress are not considered.

IV. Optimization Routine

The multiobjective optimization is performed using a genetic algorithm from Mathworks MATLAB®'s Global Optimization Toolbox (*gamultiobj*). A parameter set that completely describes the corresponding machine is optimized. In contrast to the multiobjective optimization for a TFM presented in [16], there is no preselection of parameters with higher importance. For all machines, a population of 100 individuals with a maximum of 100 generations is utilized. The initial population is generated by a Latin Hypercube Sampling (LHS), considering the lower and upper boundaries of the optimization parameters. The simulations are performed for a single operation point defined by the rms-current density of the coil of $J_{\mathrm{el,rms}} = 10\,\mathrm{A mm}^{-2}$ assuming a copper slot fill of 0.6 and a mechanical speed of $30\,\mathrm{min}^{-1}$. For the excitation of the coil a Field-Oriented-Control with pure i_q-current is utilized.

For the multiobjective optimization routine, the efficiency η and the active gravimetric torque density τ are selected as objectives. Additional conditions are used for a well-designed machine. The demagnetization of the permanent magnets is restricted with a maximum proportion of $2.5\,\%$ of volume with magnetic field $|\vec{H}|$ below the knee point. This is expressed with the ratio of demagnetization $R_{\mathrm{PM,dmg}} = V_{\mathrm{PM,dmg}} V_{\mathrm{PM}}{}^{-1}$. The limit for the power factor $\cos(\varphi)$ of ≥ 0.7 is selected because of the recommendation as seen in [17]. The third criterion is the torque ripple T_{ripple} which is limited to $T_{\mathrm{ripple}} \leq 15\,\%$ of T. The summary of these objectives is presented in Table I.

There are no direct constraints considering the thermal limits or the maximum allowed loss of the machines. Due to the fixed value of the current density representing a short-term operating point, the copper loss per area copper in the slot is limited.

Table I: Summary of the output of calculation routine with optimization objectives and additional conditions

Symbol	Description	Condition
η	Efficiency [a]	$\max(\eta)$
τ	Act. gravi. torque den. [a]	$\max(\tau)$
$\cos(\varphi)$	Power factor [b]	$\cos(\varphi) \geq 0.7$
T_{ripple}	Torque ripple [b]	$T_{\mathrm{ripple}} \leq 15\,\%$
$R_{\mathrm{PM,dmg}}$	Demag. ratio [b]	$R_{\mathrm{PM,dmg}} \leq 2.5\,\%$

[a] Optimization objective
[b] Additional nonlinear condition

Under the given conditions, the optimization routine does not ensure that the machine is able to perform the robotic task with minimum cost and maximum efficiency, as for instance presented in [18]. The target of this paper's optimization is to increase the active materials' gravimetric torque density and efficiency with a given current density of the coils $J_{\mathrm{el,rms}}$ and restricted installation space regardless a minimum required torque output. Regarding the individual types of machines, there are also different number optimization parameters. The parameter-set includes a complete description of the geometry of the machines, the outer diameter d_o is fixed to the maximum value of $180\,\mathrm{mm}$. Machines with a comparatively high number of parameters may result in a less progressed optimization. Also, the boundaries of the parameter's design space are set to values expected for favorable designs.

V. Replacement of FEA by Regression Tree Model

Compared to the combined GA introduced in [19] in which the surrogate model built once does not change during optimization, in this paper, the optimization is performed with both models: the FEA model and the surrogate model. During the multiobjective genetic algorithm optimization, the FEA-model is replaced in selected generations by a prediction using a binary decision Regression Tree Model algorithm from

Mathworks MATLAB®'s Statistics and Machine Learning Toolbox (*fitrtree*) as presented in the flowchart of Fig. 3. In order to gain a first dataset, the generations $[0, 5]$ are calculated by FEA only. If there are less than 100 data-points that do not meet all conditions, the FEA-calculations are continued till the number of minimally acceptable data-points is reached. In the next step, all previous objectives and conditions of the single FEAs are normalized into an interval $[0, 1]$ with a step size depending on the size of the dataset calculated by FEA ($n_{\text{steps}} = \max(20, \lceil 0.01 \cdot n_{\text{FEAs}} \rceil)$). The intention is not to obtain exact numerical results from the regression tree, but to obtain a scale from unacceptable to satisfactory. For building the surrogate, the normalized dataset is split into $90\,\%$-training / $10\,\%$-testing data. The regression tree is optimized regarding the leaf size and is validated for accuracy with the testing data. If the conditions of accuracy are met, the FEA is replaced by the fast-solving predictive model for the next three generations. Finally, the following generation utilizes the FEA-method again in order to confirm or correct interim results obtained by the RTM and the model will be updated.

Fig. 4 displays a benchmark between the FEA and FEA&RTM mixed methods. All results of the FEA-simulations during the genetic algorithm of both methods are displayed for the OS-UI-TFM with the number of generation indicated. Due to the exceed of maximum number of generations, the tolerance critera was not meet and the final pareto fronts are not found. Due to the limited number of calculated datapoints and conducted benchmarks this method has to be validated further.

Both optimizations are performed on a personal computer with AMD Ryzen 9 5900X 12-Core CPU, NVIDIA GeForce GT 710 GPU, and $128\,\text{GB}$ of RAM. The FEA is performed via COMSOL Multiphysics® 6.0 and Mathworks MATLAB® R2021b connected via LiveLink™ for post-processing, optimization routine including build and prediction of RTM, and data handling. The duration of the complete optimization was $370.94\,\text{h}$ (FEA) versus $117.30\,\text{h}$ (FEA&RTM) which is a speed-up of $216.23\,\%$. Despite the presented methods, the optimization routine is still time-intensive and may be replaced by a further simplified model. Due to the time-intense optimization of FEA-only method, the benchmark is performed only with a single type of machine.

VI. COMPARISON OF OPTIMIZATION RESULTS AND SELECTED MACHINES

The pareto fronts resulting of the multiobjective optimization (FEA&RTM) are illustrated in Fig. 5. All machines have the same outer diameter with a varying length depending on the optimization parameters. Certain pareto fronts do not appear to be fully formed due to the exceed of maximum number of generations, but provide a good indication of the achievable ratings

The UI-TFMs achieve higher active gravimetric torque densities and higher efficiencies. Regarding both objectives, the
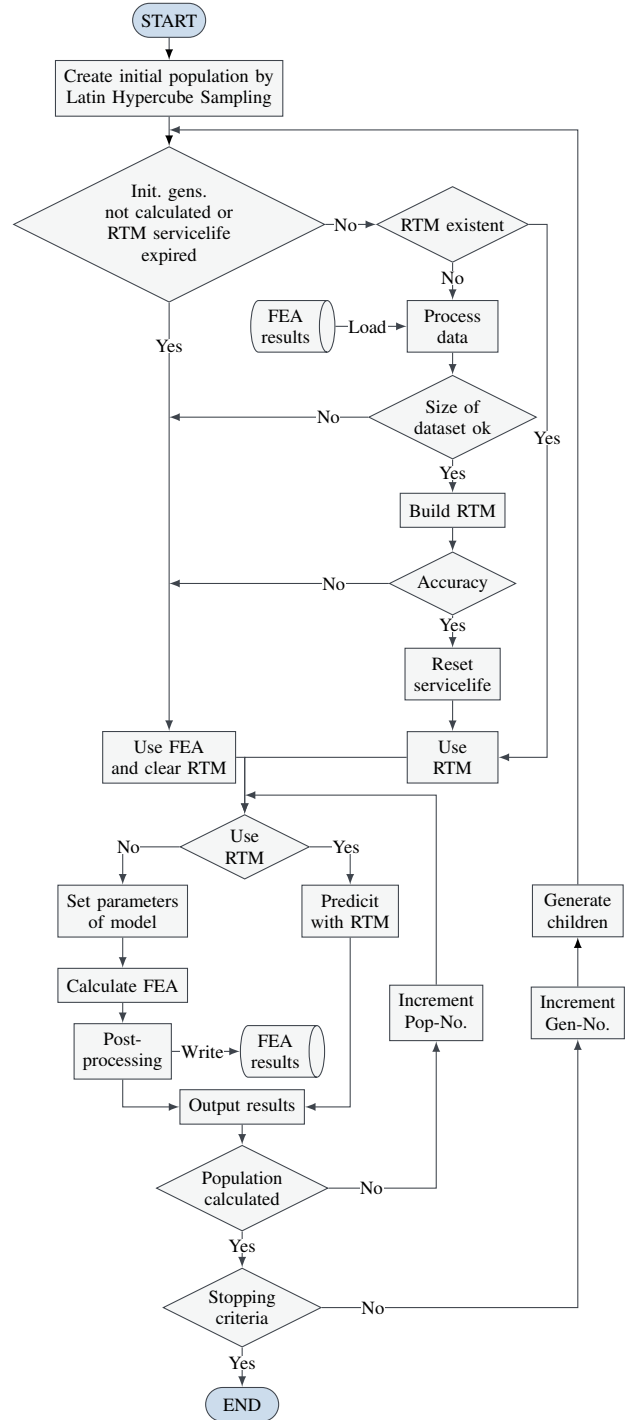

Figure 3: Schematic description of the genetic optimization routine with selective replacement of calculation by FEA with an intercalated estimation by a Regression Tree Model.

IS-UI-TFM is the superior machine. The comparison among the OS/IS/DS-TFMs also reveals the hoop coil's- and air gap diameter's impact the efficiency. The small difference of DS-CP-TFM's and OS-CP-TFM's torque density is particularly noticeable, whereas the OS-CP-TFM has the higher efficiency. For the RFMs, also the IS-RFM is superior regarding the
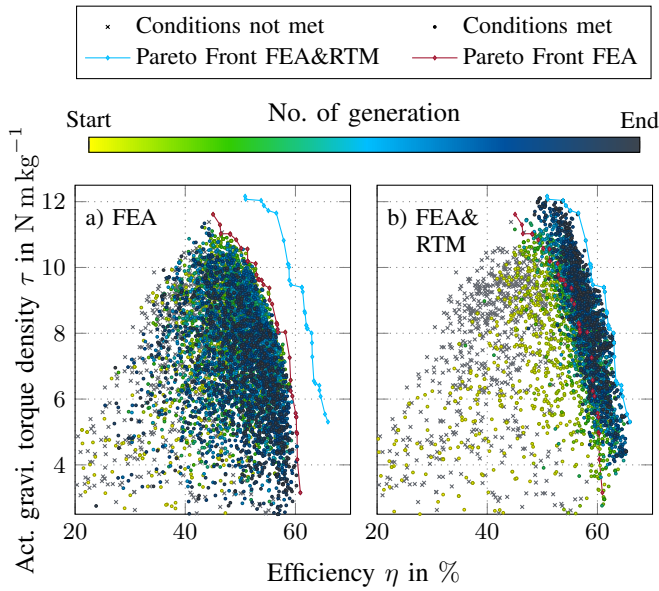
Figure 4: Results of FEAs of genetic algorithm during the optimization routine regarding the OS-UI-TFM for the conventional FEA-only method and purposed mixed FEA and Regression Tree Model method. For both, the stopping criteria was the exceed of maximum number of generations, therefore the final pareto fronts are not found, but the FEA&RTM is further progressed. The predictions from the RTM are not displayed.
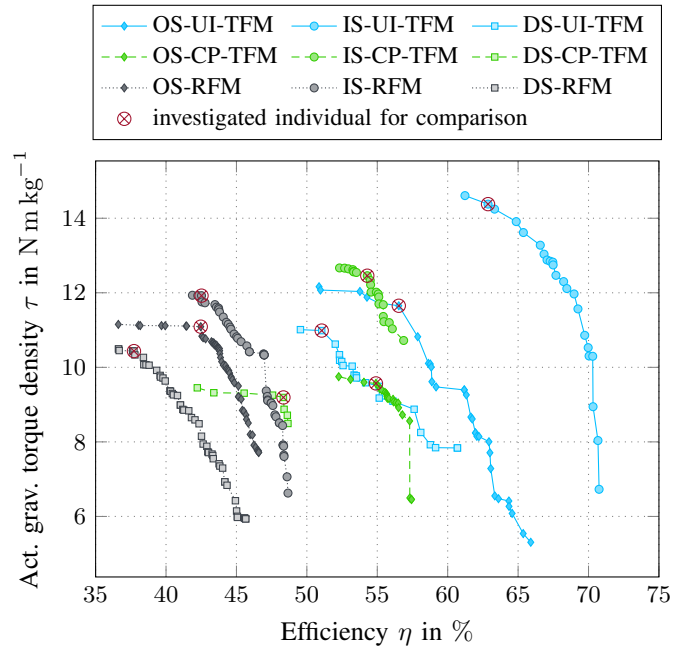

Figure 5: Resulting pareto front of single low-speed operation point by the presented mixed genetic algorithm and regression tree method from the multiobjective optimization for the studied arrangements and machines.

pareto front. For all types of machines, the DS-machines are inferior. For a further investigation selected properties of the highlighted machines selected from the pareto fronts of Fig. 5 are evaluated. In Table II this comparison is illustrated. The TFMs are inferior regarding the total torque, power factor, and specific tangential force density in the air gap regarding the RFMs with the same rotor configuration. Noticable is also the low specific tangential force density of the UI-TFMs. The utilization of the permanent magnet is similar for all machines. Regarding the loss, the TFMs are highly superior, but due to the lower total power output, the advantage is not as huge as assumed by the difference in Watts. The loss mainly consists of copper loss. Iron loss has only a small fraction of the total losses in all machines. Regarding the pole pairs, the UI-TFM's has a tendency of higher optimum numbers compared to the CP-TFM's followed by the RFM's with the lowest numbers. Regarding the length of the machines, the shorter CP-TFM's are noticeable. The air gap diameters and also the inner diameter of active material are similar for all three types of machines and rotor arrangements.

The TFM's impress with a low mass of active material, whereas the RFM's have significantly higher mass. The weight of the UI-TFM's carrier material is not included in the active gravimetric torque density. After evaluating the resulting designs of the optimization in Fig. 1 (a)-(c), there is a high

amount of air enclosed by the designs, for the UI-TFM usually filled by a carrier material lowering the total gravimetric torque density. The RFM's and CP-TFM's have no need for a carrier material. Therefore, it is not reasonable to conclude from the higher active gravimetric torque density of the UI-TFM that the total gravimetric torque density is also higher.

VII. Conclusion

The optimization with mixed methods results in an increased speed of the routine. Using the multiobjective genetic algorithm with a large population and multiple intercalated generations of the Regression Tree Model, the optimization with a high number of parameters of different relevance to the result shows better performance in the benchmark. The comparison reveals that both Transverse Flux Machines in the specified low-speed operating point have a higher efficiency and a higher active gravimetric torque density compared to the Radial Flux Machines. However, the total torque and the power factor of the Transverse Flux Machines are lower. Due to the simplified FEA in order to reduce the required calulation time for the purpose of the optimization, the results have to be validated by more detailed simulations. To conclude, the inner stator UI-core Transverse Flux Machine with high active gravimetric torque density and efficiency emerges as a suitable solution for the application as a low-speed actuator. In order to achieve a high total gravimetric torque density, an appropriate solution for the integration of the machine into the application without the need for a heavyweigth carrier is required.

Table II: Comparison of selected results and design parameters for the investigated optimized machines with the same outer diameters in the low-speed operating point.

Key-parameters	Symbol	Unit	UI-TFM			CP-TFM			RFM		
			OS	IS	DS	OS	IS	DS	OS	IS	DS
Torque	T	N m	47.6	83.3	73.8	59.2	66.2	55.0	105.8	106.7	123.2
Torque ripple	T_{ripple}	%	5.4	8.3	5.9	9.3	6.6	4.3	14.1	12.6	12.2
Act. grav. torque density	τ	$\mathrm{N\,m\,kg^{-1}}$	11.65	14.38	10.99	9.57	12.46	9.19	11.09	11.92	10.43
Torque / Inertia	T/J	$\mathrm{kN\,kg^{-1}\,m^{-1}}$	7.4	5.6	8.5	6.8	6.4	8.6	9.9	8.3	13.2
Torque / PM-mass	T/m_{PM}	$\mathrm{N\,m\,kg^{-1}}$	95.8	126.4	109.5	78.7	116.0	92.5	96.3	116.2	134.1
Spec. tang. force density OS	σ_{OS}	$\mathrm{kN\,m^{-2}}$	13.4	N/A	11.7	17.9	N/A	14.8	21.7	N/A	17.4
Spec. tang. force density IS	σ_{IS}	$\mathrm{kN\,m^{-2}}$	N/A	18.1	8.9	N/A	20.8	8.0	N/A	20.7	11.2
Copper loss	$P_{\mathrm{L,Cu}}$	W	114.1	155.6	216.8	159.9	174.3	192.8	451.8	450.9	637.1
Iron loss	$P_{\mathrm{L,Fe}}$	W	5.4	7.7	5.1	2.6	3.0	2.0	3.1	4.2	4.3
Efficiency	η	%	56.53	62.86	51.06	54.91	54.29	48.34	42.47	42.52	37.72
Power factor	$\cos(\varphi)$	-	0.79	0.71	0.73	0.80	0.70	0.79	0.99	0.99	0.99
Pole pairs	p	-	45	44	44	29	35	40	22	29	25
Ratio	$d_{\mathrm{o}}/l_{\mathrm{act}}$	-	1.52	1.57	1.51	1.69	2.21	2.29	1.34	1.58	1.50
Ratio	$d_{\mathrm{i}}/d_{\mathrm{o}}$	-	0.77	0.71	0.62	0.76	0.73	0.66	0.79	0.76	0.69
Act. length	l_{act}	mm	118.34	114.78	119.28	106.82	81.41	78.68	134.62	114.12	120.22
Air gap diameter OS	$d_{\delta,\mathrm{OS}}$	mm	146.94	N/A	151.15	148.36	N/A	154.47	152.66	N/A	155.74
Air gap diameter IS	$d_{\delta,\mathrm{IS}}$	mm	N/A	169.66	139.12	N/A	169.56	142.22	N/A	170.78	145.55
Active mass	m_{act}	kg	4.08	5.79	6.72	6.19	5.32	5.98	9.54	8.95	11.81

REFERENCES

[1] R. Dhaouadi, F. H. Ghorbel, and P. S. Gandhi, "A new dynamic model of hysteresis in harmonic drives," *IEEE Transactions on Industrial Electronics*, vol. 50, no. 6, pp. 1165–1171, 2003.

[2] J. Pippuri, A. Manninen, J. Keranen, and K. Tammi, "Torque density of radial, axial and transverse flux permanent magnet machine topologies," *IEEE Transactions on Magnetics*, vol. 49, no. 5, pp. 2339–2342, 2013.

[3] G. Lei, J. Zhu, Y. Guo, C. Liu, and B. Ma, "A review of design optimization methods for electrical machines," *Energies*, vol. 10, no. 12, p. 1962, 2017.

[4] G. Viktor, O. Dobzhanskyi, G. Rostislav, and R. Gouws, "Improvement of transverse-flux machine characteristics by finding an optimal air-gap diameter and coil cross-section at the given magneto-motive force of the pms," *Energies*, vol. 14, no. 3, p. 755, 2021.

[5] T. Reichert, T. Nussbaumer, and J. W. Kolar, "Torque scaling laws for interior and exterior rotor permanent magnet machines," in *IEEE International Magnetics Conference 2009 (INTERMAG 2009)*, Sacramento, CA, USA, 2009.

[6] E. Schmidt, "Application of a domain decomposition algorithm in the 3d finite element analysis of a transverse flux machine," in *IEEE CCECE2002. Canadian Conference on Electrical and Computer Engineering. Conference Proceedings (Cat. No.02CH37373)*. IEEE, 12-15 May 2002, pp. 156–161.

[7] A. Elantably and A. Masmoudi, "An approach to sizing high power density tfpm intended for hybrid bus electric propulsion," *Electric Machines & Power Systems*, vol. 28, no. 4, pp. 341–354, 2000.

[8] Franka Emika GmbH, "Franka control interface (fci)," accessed: 12.01.2023. [Online]. Available: https://frankaemika.github.io/docs/

[9] B. Kaiser and N. Parspour, "Transverse flux machine—a review," *IEEE Access*, vol. 10, pp. 18 395–18 419, 2022.

[10] J. F. Gieras, "Performance characteristics of a transverse flux generator," in *IEEE International Conference on Electric Machines and Drives, 2005*. IEEE, 15.05.2005 - 15.05.2005, pp. 1293–1299.

[11] M. R. Harris, G. H. Pajooman, and S. M. Abu Sharkh, "Performance and design optimisation of electric motors with heteropolar surface magnets and homopolar windings," *IEE Proceedings - Electric Power Applications*, vol. 143, no. 6, p. 429, 1996.

[12] M. Keller, S. Muller, and N. Parspour, "Design of a transverse flux machine as joint drive for an articulated six-axis robot arm," in *2016 International Symposium on Power Electronics, Electrical Drives, Automation and Motion (SPEEDAM)*. IEEE, jun 2016.

[13] J. Fischer, M. Schmid, and N. Parspour, "Investigation of maximum torque per ampere and maximum efficiency control strategies of a transverse flux machine," in *2020 International Conference on Electrical Machines (ICEM)*, vol. 1, 2020, pp. 2527–2532.

[14] S. Müller, M. Siegle, M. Keller, and N. Parspour, "Loss calculation for electrical machines based on finite element analysis considering 3d magnetic flux," in *2018 XIII International Conference on Electrical Machines (ICEM)*. IEEE, 9/3/2018 - 9/6/2018, pp. 1246–1252.

[15] S. Müller, M. Keller, A. Enssle, A. Lusiewicz, P. Präg, D. Maier, J. M. Fischer, and N. Parspour, "3d-fem simulation of a transverse flux machine respecting nonlinear and anisotropic materials," in *Comsol Conference 2016*, COMSOL, Ed., 2016, pp. 1–6.

[16] B. Zhang, A. S. Wang, and M. Doppelbauer, "Multi-objective optimization of a transverse flux machine with claw-pole and flux-concentrating structure," *IEEE Transactions on Magnetics*, vol. 52, no. 8, pp. 1–10, 2016.

[17] P. Anpalahan, J. Soulard, and H.-P. Nee, "Design steps towards a high power factor transverse flux machine," in *in Proc. European Conf. on Power Electronics and Applications*, 2001.

[18] S. Andersson, *Optimization of a servo motor for an industrial robot application*. Lund: Universitetstryckeriet, Lund University, 2000, ISBN 91-88934-15-2.

[19] M.-S. Kwon and D.-K. Lim, "Combined random forest and genetic algorithm for optimal design of pma-synrm for electric vehicles," in *2022 IEEE 20th Biennial Conference on Electromagnetic Field Computation (CEFC)*. IEEE, 24.10.2022 - 26.10.2022, pp. 1–2.